Effect of energy deposition on the disordering kinetics in dual-ion beam irradiated single-crystalline GaAs

A. Debelle, G. Gutierrez, Alexandre Boulle, I. Monnet, L. Thomé

Effect of energy deposition on the disordering kinetics in dual-ion beam irradiated single-crystalline GaAs

A. Debelle[1,2], G. Gutierrez[2], A. Boulle[3], I. Monnet[4], L. Thomé[1]
[1]Université Paris-Saclay, CNRS/IN2P3, IJCLab, 91405 Orsay, France.
[2]Université Paris-Saclay, CEA, Service de Recherches de Métallurgie Physique, 91191 Gif-sur-Yvette, France
[3]IRCER, CNRS UMR 7315, Centre Européen de la Céramique, 12 rue Atlantis, 87068 Limoges Cedex, France
[4]Normandie Univ, ENSICAEN, UNICAEN, CEA, CNRS, Centre de recherche sur les Ions, les matériaux et la photonique, 14000 Caen, France

Corresponding author: Aurélien Debelle, aurelien.debelle@ijclab.in2p3.fr

Abstract

The damage induced in GaAs crystals irradiated with dual-ion beam (low-energy I^{2+} and high-energy Fe^{9+}), producing simultaneous nuclear (S_n) and electronic (S_e) energy depositions, was investigated using several characterization techniques. Analysis of the damage buildup shows that S_n alone (single 900 keV ion beam) leads, in a two-step process, to full amorphization of the irradiated layer (at a fluence of 1.5 nm^{-2}) and to the development of a high (2.2 %) elastic strain. Conversely, only one step in the disordering process is observed upon dual-ion beam irradiation (i.e. 900 keV I^{2+} and 27 MeV Fe^{9+}, S_n&S_e); hence, amorphization is prevented and the elastic strain remains very weak (below 0.2 %). These results provide a strong evidence that, in GaAs, the electronic energy deposition can induce an efficient dynamic annealing of the damage created in collision cascades formed during nuclear energy deposition.

I. Introduction

For many years, gallium arsenide (GaAs), which is one of the most useful semiconductors of the III-V group, has been referred to as "the semiconductor of the future, and it will always be that way", because producing GaAs-based devices was complex [1]. However, in the early 2000's, advances in mobile telephony, compact-disc technology, and fibreoptic communications have boosted investments in GaAs research and development, leading to significant progresses in materials and fabrication technology. Originally, the interest in GaAs arose from its unusual band structure (as compared to that of Si for instance), which exhibits several features interesting for many electronics and optoelectronics applications (see [2] for a review). For instance, a direct band-gap results in efficient emission of photons and GaAs has then become the base material for efficient infra-red light-emitting diodes (LEDs) [3]. Due to a low effective mass, free electrons in GaAs are very mobile under the influence of an electric field, resulting in fast devices, a property used in, e.g., high-energy particle detectors [4]. A further characteristic of great interest in GaAs, not related to its band structure, is that the lattice parameters of GaAs and aluminum arsenide (AlAs) are very close, which allows growing various alloys and heterostructures without suffering from defect creation due to lattice mismatch. Such GaAs-based heterostructures are currently the new path of development of GaAs devices, notably for solar cells [5, 6]. For most of these uses, and also for functional design (such as doping), GaAs is subjected to energetic particle (mainly ion) irradiation, a phenomenon during which complex energy deposition processes are involved. These processes may lead to complex, intricate modifications of the material microstructure ultimately degrading the materials properties.

Ion irradiation is a phenomenon during which energetic charged particles interact with solids, thereby progressively losing their energy according to two distinct processes that depend on their velocity [7]. A projectile with a low velocity (as compared to the root-mean square velocity of its own electrons) essentially interacts with matter through elastic - so-called nuclear or ballistic - collisions with the (screened) nuclei of the target atoms. During this kind of collisions, a fraction of the projectile kinetic energy is transferred to target atoms and, if this transferred energy is larger than a threshold displacement energy (E_d), the knock-on atom is ejected from its lattice site; the associated slowing-down process is related to the nuclear stopping power (S_n), and S_n hereafter denotes the ballistic collision regime. Note that if the velocity of the recoil atom is sufficient, this latter can induce collective displacements of

target atoms, a phenomenon referred to as a collision cascade [7]. Opposite to low-velocity ions, swift ions essentially interact with electrons of the target atoms, inducing excitation and ionization processes, and this slowing-down is related to the electronic stopping power (S_e); hereafter, we use S_e to refer to the ionization regime. It is important to mention that a significant amount of the energy deposited to the electrons can reach the atomic network through an electron-phonon coupling, which may produce atomic displacements, particularly in iono-covalent materials [7]. Acquiring a better knowledge of the energy partitioning between the electronic and atomic networks constitutes an important issue to address, which is in fact the case (see [8] and references therein for a short review of that very topic). The main reason for this interest, apart from that it better reproduces some real in-service conditions (like for particle detection or aerospace applications), is that coupled - hereafter denoted as S_n&S_e - effects can take place, and they are frequently referred to as *synergistic effects* because the result is not the algebraic sum of the different contributions. On the contrary, for semiconductors like Si and SiC for instance, S_e has been found to heal crystals disordered by S_n [8-10 and references therein]. A comprehensive description and understanding of these complex phenomena may facilitate the design of materials with tailored properties and prolonged lifespan. One possibility to address this subject consists in performing dual-beam irradiation experiments (i.e. with two different ions) where both S_n and S_e components are present and perfectly controlled.

This paper does not intend to provide a detailed review of radiation effects in GaAs. Yet, we can mention that experimental works demonstrated that GaAs is easily damaged by nuclear collisions (S_n) and undergoes amorphization, when irradiated at room temperature (RT), at a fraction of displacement per atom (dpa) [11-13] (note that the AlGaAs alloy exhibits a higher resistance with increasing the Al content [13]). Computational modelling confirmed this result and provided atomistic information about the nature of the radiation defects that are essentially of interstitial type and in the form of small clusters [14-15], but another work reported the formation of Frenkel pairs only [16]. In any case, increase in density of these defects leads to increase in the free energy until the crystalline structure collapses into an amorphous phase. It is important to emphasize that a dynamic annealing process can take place as soon as the temperature for defect mobility is reached (around 200 K in GaAs [17]), and this annealing allows preventing amorphization at irradiation temperature as low as 333 K (as compared to about 573 K in SiC) [12-13]. Likewise, atomistic simulations showed that very

low energy recoils (about 5–10 eV) can lead to a significant recrystallization in GaAs [15]. In short, both thermal and athermal efficient annealing processes can occur in GaAs. This is probably why this material is particularly resistant against ionizing events occurring with high-velocity ion (S_e), laser or electron irradiation. Indeed, only point defects or small defect clusters seem to form under S_e irradiation [18-19], and the ionizing events can even induce recrystallization [20-23]. This recrystallization phenomenon has been observed in sequential irradiation experiments (S_n followed by ionization), and it is equivalent to that reported in other semiconductors.

In the present work, we show that a highly efficient defect annealing takes place in GaAs, at RT, upon dual-beam (i.e. simultaneous, in contrast to sequential) irradiation experiments; this phenomenon is referred to as SNEEL, which stands for synergy between nuclear and electronic energy-losses [24]. To reach this conclusion, we provide disordering kinetics under both S_n and S_n&S_e irradiations using three complementary characterization techniques.

II. Experimental details

This study uses undoped {100}-oriented GaAs single crystals from the MTI Corporation. Samples were irradiated at room temperature at JANNuS in Saclay [25]. A single 900 keV I^{2+} ion beam (called S_n) or a dual 900 keV I^{2+} and 27 MeV Fe^{9+} ion beam (called S_n&S_e) were used. The I^{2+} ion fluence ranged from 0.3 nm^{-2} to 5 nm^{-2}, and a ratio of 1.8 between S_e and S_n ion fluxes was applied to obtain the maximum synergistic effect [26]. A thermocouple and a thermal imaging camera were used to monitor the irradiation temperature. Simulations of the projectiles/GaAs interactions were carried out using the SRIM2011 code in the "Full Damage Cascades" mode [27], which is relevant to determine the energy loss components. For these calculations, a threshold displacement energy of 13 eV was used for both Ga and As sublattices [28]. The corresponding results are presented and commented in section III.1. For the reader convenience, the number of displacements per atom (dpa) at the SRIM-predicted damage peak (~150 nm) is given in Table I, along with all useful sample characteristics. In addition, we provide, in Appendix A, the I-induced dpa depth profile and the I ion range for the 5 nm^2 fluence. To finish, we can mention that the dpa rate (for the I irradiations) was ~2.6×10^{-3} $dpa.s^1$ at the damage peak.

Rutherford backscattering spectrometry associated to channeling (RBS/C) was done with the JANNuS-SCALP equipment at the IJClab in Orsay [25]. These experiments used 1.4 MeV He ions and a detector located at a 165°. Experimental data were reproduced with the McChasy code developed at the NCBJ in Warsaw [29]. For that purpose, it was assumed that a fraction of atoms (called f_D) are displaced in a random way from their regular site, a phenomenological approach that reasonably corresponds to the actual disordering process in GaAs.

Raman characterizations were done at the JANNUS laboratory in Saclay, with a frequency-doubled Nd:YAG (532 nm) laser in an Invia Reflex Renishaw spectrometer in the backscattering geometry coupled to a Leica microscope with a 100x objective. The power of the laser was less than 0.05 mW to prevent sample modifications, as it has been reported in the literature that such green laser light could induce recrystallization in damaged GaAs [21]. The Raman spectrometer was calibrated using silicon single crystals. The fitting module of the WiRE Raman software was employed for simulating the spectra assuming Voigt distributions.

High-resolution X-ray diffraction (HR-XRD) measurements were performed at the IRCER in Limoges with a Bruker D8 Discover. A monochromatic (λ_{Cu}=0.15406 nm) X-ray beam was employed to probe the 004 Bragg reflection by performing θ-2θ scans (2θ being the Bragg angle for diffraction). Experimental curves were fitted using the RaDMaX-Online code [30-31]. Both elastic-strain (ε) and static Debye-Waller (DW) depth profiles were determined from those simulations.

Transmission electron microscopy (TEM) experiments were performed at CIMAP in Caen, on a selection of samples using a JEOL-F200 microscope working at 200 keV. For this purpose, cross-sections were synthesized with a focused-ion-beam using a Helios Nanolab 660 equipped with Ga^+ ions accelerated at 30 keV. Bright-field images were recorded, as well as electron diffraction (SAED) patterns collected with a 10 µm aperture diaphragm.

It must be mentioned here that all samples were irradiated during the same campaign, in one set for S_n irradiations and in another set for S_n&S_e irradiations, except for the 5 nm^{-2} fluence which was obtained in a previous experiment (yet with as much as possible identical conditions). All samples were then characterized by RBS/C, but for Raman spectroscopy and XRD, some crystals have not been measured because of logistics issues (e.g. shipment between the different laboratories involved in the study). This explains why not all data points are present in figures relying on Raman and XRD techniques.

III. Results

III.1. SRIM calculations

The S_n and S_e depth profiles of 900 keV I^{2+} and 27 MeV Fe^{9+} ions are presented in Figure 1. Note that only the first 500 nm are shown in this figure since such a thickness concerns the region perturbed by I^{2+} ions. The maximum of $S_n(I)$ reaches 3 keV/nm, a value which is sufficient to induce, *via* collision cascades, significant damage in the form of defect and defect clusters [11-13]. $S_e(I)$ remains below 1 keV/nm, a low value that still could induce defect annealing in GaAs. This component is always present (*i.e.*, for S_n and $S_n\&S_e$ irradiations), so that its potential influence is included in all experiments and it will not hamper the monitoring of the expected $S_e(Fe)$ effect. Regarding precisely $S_e(Fe)$, it is almost constant over the first micron and it reaches ~7.5 keV/nm, a value which is sufficiently high to induce damage annealing, as mentioned in the Introduction (see also [18]) and as demonstrated in the following sections. $S_n(Fe)$ stays below 0.1 keV/nm and can therefore be neglected for defect creation, at least as observed by RBS/C (see Appendix B), but not completely for XRD measurements (see section III.4.).

III.2. RBS/C results

RBS/C spectra recorded on GaAs single crystals irradiated with either single 900 keV I^{2+} ion beam or dual-ion beam of 900 keV I^{2+} and 27 MeV Fe^{9+} ions are presented in Figure 2 (a,b). The damage fractions (f_D), obtained from simulations of RBS/C spectra using the McChasy code, are also shown in Figure 2 (c,d).

For single I^{2+} ion irradiation, spectra exhibit a defect peak at 150 nm. This maximum corresponds to the SRIM-predicted dpa peak (see Appendix), and furthermore, the RBS/C-derived disorder profiles look very similar to the SRIM-predicted one. As the mean projected range of I ions is around 230 nm, those findings strongly suggest that the detected disorder is essentially related to defects induced by nuclear collisions of I ions with the GaAs target atoms, and no specific effect of injected interstitials or incorporated (iodine) impurities is observed. The intensity of the damage peak increases with increasing I^{2+} fluence, and it attains the random level (f_D=1) at 0.7 nm^{-2}. This result suggests that amorphization of the irradiated layer starts at this depth and at this I^{2+} fluence. At higher fluences, the amorphous layer expands towards the surface and the bulk.

Much less damage is observed in crystals irradiated with dual-ion beam of I^{2+} and Fe^{9+} at I^{2+} fluences similar to those used in the case of I^{2+} irradiation alone. Moreover, amorphization of GaAs crystals is prevented, even at the largest I^{2+} fluence (5 nm^{-2}) for which f_D remains very small (<0.1) in the irradiated layer. Thus, it can be concluded that a strong effect of S_n/S_e synergy occurs in GaAs irradiated with dual-ion beam.

III.3. Raman results

Raman spectra recorded on pristine and ion-irradiated (S_n and $S_n\&S_e$) GaAs single crystals are shown in Figure 3. For our excitation wavelength (532 nm), the probing depth of the laser is less than the region perturbed by I^{2+} ions (< 500 nm). The Raman spectra collected at the sample surface thus correspond to a region where the two beams interact (for the $S_n\&S_e$ irradiation). For the pristine sample, one band with a high intensity is visible at 290.8 cm^{-1} corresponding to the longitudinal optical (LO) mode due to the phonon scattering in a perfect crystalline GaAs [32]. A weaker band at 267.5 cm^{-1} associated to the transverse optical (TO) phonon band is also observed. Irradiation with low-velocity ions alone (S_n) induces a significant modification of the spectrum (Fig. 4(a)): the LO and TO bands progressively disappear with increasing the I^{2+} fluence, at the expense of a broad peak at about 250 cm^{-1} (a-GaAs) that originates from an amorphous phase [32-33]. Before complete disappearance of the LO mode, a shift towards lower wave numbers is clearly noticed, revealing a disordering of the crystalline structure prior to the collapse into the amorphous phase. For the dual-beam irradiation ($S_n\&S_e$), the LO and TO bands are still present at the highest used I^{2+} fluence (Fig. 4(b)), in agreement with the absence of amorphization evidenced by RBS/C. A shift of the LO band towards lower wave numbers (by 4.2 cm^{-1}) is, as for the S_n irradiation, observed, accompanied by a broadening (FWHM) of 5 cm^{-1}. These latter changes reveal some degree of disorder in the crystalline phase. Therefore, as evidenced below by XRD, a mixture of crystalline and weakly damaged regions is present in the GaAs irradiated with dual-ion beam.

III.4. XRD results

θ-2θ scans recorded from the 400 reflection of GaAs for the S_n and $S_n\&S_e$ cases are displayed in Figs. 4(a) and 4(b), respectively. The experimental data (gray circles) shows the Bragg peak of bulk GaAs at 2θ = 66.05° which originates from the virgin part of the crystal underneath the irradiated region. Indeed, the attenuation length of the CuKα$_1$ radiation in

GaAs is ~15.3 µm (1/e attenuation) at an angle corresponding to the 400 reflection, which means that the incident beam travels through the damaged layer and reaches the pristine crystal, even in the S_n&S_e case. At lower angles, an additional signal is visible that is related to the presence of a dilatation gradient in the direction normal to the surface [34-35]. The comparison of Fig. 4(a) with Fig. 4(b) shows that in the latter, the 2θ range spanned by the additional signal is less than in the former, which readily suggests that the overall level of strain is weaker in the S_n&S_e case than it is in the S_n case.

More in-depth information can be obtained by the simulation of the XRD curves. RaDMaX simulations [28-29] are shown as colored lines in Figs 4(a) and 4(b) and the corresponding results are given in Figs. 4(c) and 4(d) for the the S_n and S_n&S_e cases, respectively. It should be mentioned that such simulations allow to retrieve both the lattice strain and the disorder. However, since the latter is here determined by both RBS/C and Raman spectroscopy, we shall solely focus on the strain. The strain depth profiles for S_n irradiations (Fig. 4(c)) show that the strain is concentrated in a ~400 nm sub-surface region, with a maximum located at ~150 nm (consistent with RBS/C results), but with a profile tail expanding down to ~900 nm (i.e. deeper than the disorder profile determined by RBS/C, suggesting a higher sensitivity of the XRD technique for such weakly defective crystalline regions). At 0.3 nm^{-2}, the maximum strain is 0.86 % and it reaches 2.26 % at 5 nm^{-2}. The S_n&S_e case is much more challenging to simulate, since the strain and disorder depth profiles contain contributions from the stopping powers of both projectiles (including the $S_n(Fe)$ component). The complete strain profiles then extend down to 8 µm below the surface, but for the sake of comparison with the S_n case and with the three other techniques, only the first 900 nm are shown in Fig. 4(d). It can clearly be observed that the level of strain is much weaker in the S_n&S_e case than it is for the sole S_n irradiation (0.8 % vs 2.35 % at 5 nm^{-2} for instance), indicating that the defect annealing already evidenced for the damage fraction (RBS/C) also affects the elastic strain.

III.5. TEM results

Figure 5(a) presents a cross-section view of a GaAs sample irradiated with 900 keV I^{2+} ions (S_n only) at the fluence of 5 nm^{-2}. After the platinum layer deposited at the sample surface to protect it during the cross-section preparation, an amorphous layer is clearly visible (as attested by the SAED pattern that shows continuous rings only). It extends from the surface

to a depth of ~395±10 nm, in agreement with RBS/C results. Below this amorphous layer, some defect clusters (so-called black dots) can be observed, and can be related to the tail of the I^{2+} projectile distribution where the dpa level was not high enough to induce a full amorphization; this finding is consistent with the tail in the strain profile as shown in Fig. 4(c). Deeper also are visible some larger black dots, but these ones are most likely originating from the FIB preparation process, as checked on a prepared pristine crystal. After the damaged zone, one can observe a perfect crystal as indicated by the SAED pattern. The cross-section in Fig. 5(b) corresponds to the GaAs crystal irradiated with both Fe^{9+} and I^{2+} ions (S_e&S_n) at the same I^{2+} fluence as for Fig. 5(a) (i.e for S_n only). The microstructure appears strikingly different from that of the S_n-irradiated crystal (Fig. 5(a)). There exists no amorphous layer, as expected from the RBS/C, XRD and Raman results; the only visible contrast reveals a weak damage in the irradiated layer. This statement is corroborated by the SAED pattern exhibiting slightly diffuse spots.

IV. Discussion

IV.1. Modelling of the damage build-up

The RBS/C, Raman and XRD data presented in the previous section allow to derive disordering kinetics, *i.e.*, the variation, as a function of the iodine ion fluence, of a parameter that describes the irradiation-induced effects on the microstructure of irradiated single crystals. For RBS/C and Raman (Figs. 6 and 7, respectively), damage fractions (f_D) were used, and, for XRD, the elastic strain (ε) was preferred (see Fig.8) as its determination is more robust than that of the XRD-derived disorder level [30]; moreover, the disorder is already assessed by the two other techniques. In the case of RBS/C (XRD) data, the disorder (strain) was monitored at the depth where the damage (strain) is maximum, *i.e.*, around 150 nm; for Raman data, the disorder is integrated over the entire depth probed by the laser, which is around 150 nm in GaAs [36].

As reported in several works where irradiation conditions similar to those used in the current study were employed, the amorphization process of GaAs crystals in the S_n regime should proceed in two steps, irrespective of the characterization technique (RBS/C [33], Raman [33] and XRD [37]). Therefore, to fit the disordering kinetics that we obtained with the three techniques, we used a dedicated model, called Multi-Step Damage Accumulation (MSDA) model [38]. This model is described by the following equation:

$$D=\sum_{i=1}^{n-1}\left\{D_i^{sat}\ G\left[1-\exp(-\sigma_i(\Phi-\Phi_i))\right]\prod_{k=1}^{n}\left[\exp\left(-\sigma_{k+1}\left(\Phi-\Phi_{k+1}\right)\right)\right]\right\}+D_n^{sat}G\left[1-\exp\left(-\sigma_n\left(\Phi-\Phi_n\right)\right)\right] \quad (1)$$

where D corresponds to the studied disorder parameter (f_D or ε) and D^{sat} is the associated value at saturation, n is the number of steps required for the achievement of the total disordering process, Φ_i is the threshold (I^{2+}) ion fluence of the i^{th} step, and σ_i the corresponding disordering cross-section. *G(x)* corresponds to the Heaviside function *H(x)* multiplied by its argument (*i.e.*, xH(x)). In Figures 6 to 8, fitting curves to experimental data with Eq.(1) are displayed as solid blue lines for the S_n irradiations, and as solid red lines for the S_n&S_e irradiations. The fitting parameters are listed in Table II. It must be emphasized that, considering the different sensitivities of the techniques used and the lack of data points at low fluence, any quantitative interpretation of the values found for these parameters must be cautious.

Figure 6 presents the damage buildup using RBS/C (i.e. $D = f_D^{RBS}$ as a function of the I^{2+} ion fluence) obtained from the data shown in Figure 2. In the case of I^{2+} ion irradiation alone (S_n), the amorphization kinetics is correctly described using two steps, *i.e.*, n=2 in Eq.(1) (the fit was much less accurate considering a one-step process). In the inset of Fig.6 are displayed the experimental data and the fitted disordering kinetics in log-scale. Such a representation provides the advantage to highlight the two steps of the disordering process. Obviously, it is found that $f_{D,sat-2}^{RBS}(S_n) = 1$, consistently with a full amorphization of the irradiated layer.

Regarding the disordering kinetics obtained from Raman spectroscopy, the damage fraction, $D = f_D^{RAMAN}$, was calculated considering the intensity of the two bands characteristic of the presence of disordered regions (*i.e.*, the TO and a-GaAs bands shown in Fig.3). For this purpose, the Raman peaks were fitted with pseudo-Voigt functions and the global damage fraction was estimated as follows:

$$f_D^{RAMAN} = \left(I_{a-GaAs} + I_{TO}\right) / I_{LO} \qquad (2)$$

where I_{LO}, I_{TO} and $I_{a\text{-}GaAs}$ represent the integrated intensities of the LO, TO and a-GaAs bands, respectively. This procedure has already been used elsewhere [33]. Note that Raman data are averaged over ~150 nm or less [36] that depends on the disorder level) below the surface, which necessarily includes less disordered areas than those probed at the damage peak only, as it was the case for RBS/C and XRD. Figure 7 presents the variation of f_D^{RAMAN} with the I^{2+} ion fluence. As the LO band is no longer visible at fluences above 1.5 nm^{-2}, we decided to consider that amorphization started at this fluence; hence, we normalized the f_D^{Raman} values to the value determined at this fluence (i.e. f_D^{Raman} =1 at 1.5 nm^{-2}). Clearly, a correct fit of the experimental data can again be obtained considering two steps in the amorphization process (see solid blue line in Fig.7). The accuracy of the first step is here also limited, as shown in the inset of Fig.7 that presents, in log-scale, the two components of the disordering kinetics. Necessarily, $f_{D,sat-2}^{Raman}(S_n)$ is equal to 1.

The strain build-up was derived from XRD simulations. For this purpose, the strain values observed in the 100-200 nm range (Fig. 4(c-d)) were averaged and plotted *vs* the I^{2+} ion fluence (see Fig. 8). As it was already deduced for the damage fractions extracted from RBS/C and Raman spectroscopy data, the strain kinetics for the sole S_n irradiation can be described with a two-step model (n=2 in Eq.(1), with $D = \varepsilon$ - see the inset in log scale). The strain level at

saturation, $\varepsilon_{sat-2}(S_n) = 2.2\%$, is about three times higher than the values reported in [37]. This discrepancy most likely comes from the data analysis procedure. Indeed, in [37] the strain was derived from the position of the last fringe in the XRD signal whereas in the current work we used a data simulation procedure [30-31] to fully fit the signal, which provides more accurate results (on the strain), particularly when the intensity is low (*i.e.*, at the damage peak).

In contrast to S_n irradiations, the variation of f_D^{RBS} upon dual-beam irradiation (S_n&S_e) was fitted (red line in Fig.6) assuming a one-step model (usually referred to as direct impact mechanism which is in fact a Poisson distribution). This feature is a key difference in the two different disordering processes, as discussed hereafter. In this case, we obtain $f_{D,sat}^{RBS}(S_n \& S_e) = 0.06$, which means that even at the highest fluence (5 nm^2), the disorder level remains very weak, confirming that part of the defects created by S_n are annealed by the Fe^{9+} ion beam. Likewise, $f_{D,sat}^{Raman}(S_n \& S_e) = 0.18$ while it is 1 for the sole S_n irradiation. A same dramatic decrease is observed for the strain at saturation: $\varepsilon_{sat}(S_n \& S_e) = 0.5\%$, a value four times lower than that determined for the sole S_n irradiation, evidencing a lesser defect density. Yet, this strain level (at saturation) is significant, in contrast to the RBS/C or Raman disorder levels for which very little disorder is detected; such a discrepancy is discussed hereafter.

The above-presented set of results clearly indicates that a different disordering process takes place upon single or dual-ion beam irradiations. During S_n irradiation, amorphization occurs via a two-step process. Firstly, point defects and associated clusters are created. These defects must be predominantly of interstitial-type, as RBS/C is highly sensitive to them, and since interstitial defects in GaAs do induce a positive strain because they exhibit a positive relaxation volume [39]. Besides, atomistic simulations pointed out that both vacancy and interstitial clusters are formed in collision cascades, but interstitial clusters are bigger and more numerous [40-41]. Secondly, amorphous-like clusters form, surrounded by defective but still crystalline regions that eventually transform into an amorphous state (hence the detected strain that increases up to full amorphization). This scenario, already proposed in the literature, matches with our results obtained with the three techniques. During S_n&S_e irradiation, only one step is observed, and no amorphization takes place. Therefore, it is very likely that the second step of the disordering process evidenced during the S_n irradiation is suppressed, and only point defects and associated small clusters are formed. This picture is consistent with the results provided by the three techniques, particularly the fact that the

RBS/C disorder is very low, even though the elastic strain remains appreciable (although considerably reduced). Indeed, as shown in [39], interstitial point defects in GaAs have a large relaxation volume (~1.5 atomic volume). Therefore, $\varepsilon_{sat}(S_n \,\&\, S_e) = 0.5\%$ (for S_n&S_e irradiation) would correspond, if all defects were point defects (and considering the mechanical reaction of the non-irradiated part of the GaAs crystal [34]), to a ~0.5 % concentration, which is hardly detectable by RBS/C, but is by XRD. Thus, a fundamental question arises from the results presented above: why is the second step suppressed upon dual-ion beam irradiations?

IV.2. Tentative explanation of the dynamic damage annealing

GaAs is known to be barely damaged by inelastic collisions, as demonstrated in different works where either magnetic [42] or structural [13,18,43] properties were monitored upon swift heavy ion irradiation. Ion tracks were observed only in the case where S_e exceeds a threshold value of ~33 keV/nm [19,44]. Another important potential effect of electronic energy deposition in GaAs is a damage annealing. Indeed, several studies reported such a phenomenon induced by either electromagnetic waves (*e.g.* laser) or energetic particles (100^{ths} of keV electrons or ions in the MeV range or higher) [18,21,22,45-47]. However, as previously observed in, *e.g.*, Si [10], the annealing efficiency is much greater upon simultaneous irradiation (S_n&S_e) than during sequential irradiations (referred to as S_n+S_e) that represent the vast majority of experiments reported in the literature. For instance, for sequential irradiations with S_e around 23 keV/nm, *i.e.*, three times larger than in the current work, the annealing efficiency was found to be high (~80 %), but not as much as that observed here (almost 100 %) [48]. Moreover, this high value was obtained for a pre-damage level $f_D^{RBS} < 0.75$. To verify that dual-ion beam irradiation is more efficient than sequential irradiations in preventing amorphization, we have also performed sequential irradiations (*i.e.*, Fe subsequently to I) in the present work. The results (see Appendix) reveal that only a slight shrinkage of the amorphous layer produced by S_n irradiation occurs as a result of the effect of S_e irradiation. These additional experiments confirm the lower annealing capability of sequential irradiations, although there is no spatial and time overlapping between S_n and S_e impacts during S_n&S_e [49].

Several explanations have been proposed to explain the damage annealing induced by electronic energy deposition, which include beam heating, displacements of atoms, bond breaking, and local excitations (as reported for instance in [40]). Bond breaking (because of excitations leading to antibonding states) and subsequent migration of the dangling bonds, as described in the Spaepen-Turnbull model of recrystallization at interfaces [50], appears to be the most accepted interpretation of the annealing phenomenon. Yet, if this geometric rearrangement during the time where the bond is broken was the only annealing process to take place, then sequential and simultaneous ion irradiation experiments should lead to a similar recovery, which is clearly not the case. Therefore, we suggest that, in addition to bond rupture and reformation in a regular tetrahedral configuration of the diamond-like structure, defect migration leading to their annihilation and/or recombination should also be considered as a potential dynamic (i.e. during the irradiation process) recovery mechanism. Indeed, the defect mobility can be enhanced due to the thermal energy brought to the atomic network through an electron-phonon coupling during inelastic interactions. This process is accounted for in the so-called thermal spike model [51]. This annealing mechanism has already been put forward to explain the irradiation-induced recrystallization of other materials, including semiconductors [52-54]. In addition, it has been shown that recrystallization of damaged GaAs is possible at 250 K [55], a temperature which is likely reached inside 27 MeV Fe^{9+} tracks. To schematize this process, one could imagine that an iodine ion (S_n) would produce point and small defect clusters (the cross-sections given in Table II suggest diameters of a few nm for these defects, that are consistent with previous TEM observations [55]). Then, an Fe^{9+} ion (S_e) would travel through these clusters, locally increasing significantly the temperature, thereby allowing defect annealing and, hence, a recovery of the crystalline lattice. It is to be noted that such a recrystallization process requires the presence of surrounding crystalline seeds to occur [52], explaining why it takes place only at the crystalline-amorphous interface at the backside of a fully amorphous (irradiated) layer. In other words, the proposed dynamic recovery process is spatially localized along each ion track, so that it can occur efficiently on small defect clusters (those for which the required energy to be annealed out is consistent with that deposited by the swift ion), but it cannot lead to recrystallization of a sample that is already amorphized (because the amorphous state is energetically too stable, and no crystalline seed is present). As a matter of fact, no recrystallization inside ion tracks have been reported so far in amorphous GaAs.

V. Conclusion

The disordering process occurring in ion-irradiated GaAs crystals was investigated in a particularly interesting context where two different irradiation configurations were used: (i) 900 keV I^{2+} ions for which the nuclear stopping power (S_n) is dominant, (ii) dual-ion beam composed of 900 keV I^{2+} & 27 MeV Fe^{9+} ions so that concomitant electronic (S_e) and nuclear energy depositions occur. The disordering kinetics determined from the variation of the damage parameters obtained by RBS/C and Raman reveal that GaAs is rapidly amorphized upon S_n irradiation only, while this phase change is prevented during simultaneous irradiations. In fact, a competing mechanism between defect creation and defect annealing processes takes place during S_n&S_e irradiations, driving the microstructure to a steady-state characterized by a low defect density, and hence a low disorder level that saturates at 6 % (according to RBS/C). The strain kinetics support this description, and while the maximum strain is found to be ~2.2 % after S_n irradiation alone, it is less than 0.5 % after S_n&S_e irradiations. Sequential irradiations (S_e subsequent to S_n) also lead to a disorder annealing, but with a significantly lower efficiency than simultaneous S_n&S_e irradiations. This work could have strong implications on the design of devices integrating GaAs for radiation-harsh applications.

Acknowledgments

We would like to thank: the French EMIR&A network for providing irradiation beamtime, the JANNuS-Saclay team for performing irradiations, the JANNuS-SCALP platform staff for their help during RBS/C experiments.

Conflict of interest

Authors declare no conflict of interest.

Sample denomination	Irradiation sequence	Fluence (I) (10^{14} cm^{-2}) (nm^{-2})	dpa (I) @ 150 nm	Fluence (Fe) (10^{14} cm^{-2}) (nm^{-2})	dpa (Fe) @ 150 nm
$S_n(1)$	900 keV I^{2+} (single)	0.3	0.8	-	-
$S_n(2)$	900 keV I^{2+} (single)	0.5	1.35	-	-
$S_n(3)$	900 keV I^{2+} (single)	0.7	1.89	-	-
$S_n(4)$	900 keV I^{2+} (single)	0.9	2.43	-	-
$S_n(5)$	900 keV I^{2+} (single)	1.5	4.05	-	-
$S_n(6)$	900 keV I^{2+} (single)	3	8.1	-	-
$S_n(7)$	*900 keV I^{2+} (single)*	*5*	*13.5*	-	-
$S_n\&S_e(1)$	900 keV I^{2+} & 27 MeV Fe^{9+} (dual)	0.3	0.8	0.54	0.017
$S_n\&S_e(2)$	900 keV I^{2+} & 27 MeV Fe^{9+} (dual)	0.5	1.35	0.9	0.028
$S_n\&S_e(3)$	900 keV I^{2+} & 27 MeV Fe^{9+} (dual)	0.7	1.89	1.26	0.039
$S_n\&S_e(4)$	900 keV I^{2+} & 27 MeV Fe^{9+} (dual)	0.9	2.43	1.62	0.051
$S_n\&S_e(5)$	900 keV I^{2+} & 27 MeV Fe^{9+} (dual)	1.5	4.05	2.7	0.084
$S_n\&S_e(6)$	900 keV I^{2+} & 27 MeV Fe^{9+} (dual)	3	8.1	5.4	0.169
$S_n\&S_e(7)$	*900 keV I^{2+} & 27 MeV Fe^{9+} (dual)*	*5*	*13.5*	*9*	*0.281*

Table 1: Irradiation details of the studied crystals, including the irradiation sequence, the ion fluence(s) and the dpa level at the damage peak (i.e. at 150 nm). The two lines in italic indicate that the corresponding samples were irradiated during a previous campaign.

	Step 1 f_{D1} / ε_1 (%)*	Step 1 σ_1 (nm^2)	Step 2 Φ_2 (nm^{-2})	Step 2 f_{D2} / ε_2 (%)*	Step 2 σ_2 (nm^2)
S_n (RBS)	0.40 ± 0.30	1.0 ± 0.8	0.25 ± 0.15	1.0 ± 0.05	5.3 ± 2.0
S_n&S_e (RBS)	0.10 ± 0.02	2.1 ± 0.8	-	-	-
S_n (Raman)	0.40 ± 0.30	2.2 ± 1.0	0.56 ± 0.20	1.0 ± 0.05	2.0 ± 1.5
S_n&S_e (Raman)	0.16 ± 0.02	4.0 ± 2.0	-	-	-
S_n (XRD)	0.80 ± 0.60	2.8 ± 2.0	0.40 ± 0.20	2.2 ± 0.1	4.0 ± 2.0
S_n&S_e (XRD)	0.38 ± 0.02	5.2 ± 2.0	-	-	-

Table 2: Fitting parameters for the disordering kinetics using the MSDA model.
*f_{D1} and f_{D2} are related to RBS and Raman data. ε_1 and ε_2 (in %) are related to XRD data.

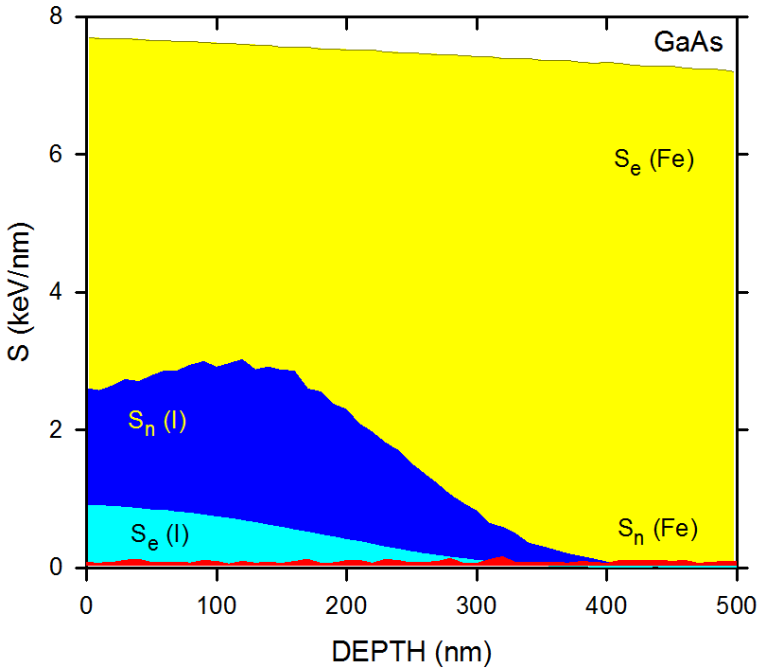

Figure 1

Depth dependence of nuclear (S_n) and electronic (S_e) stopping powers in the case of a GaAs target irradiated with 900-keV I^{2+} ions (blue and cyan areas) or 27-MeV Fe^{9+} ions (red and yellow areas). These simulations were performed with the SRIM2011 program [27].

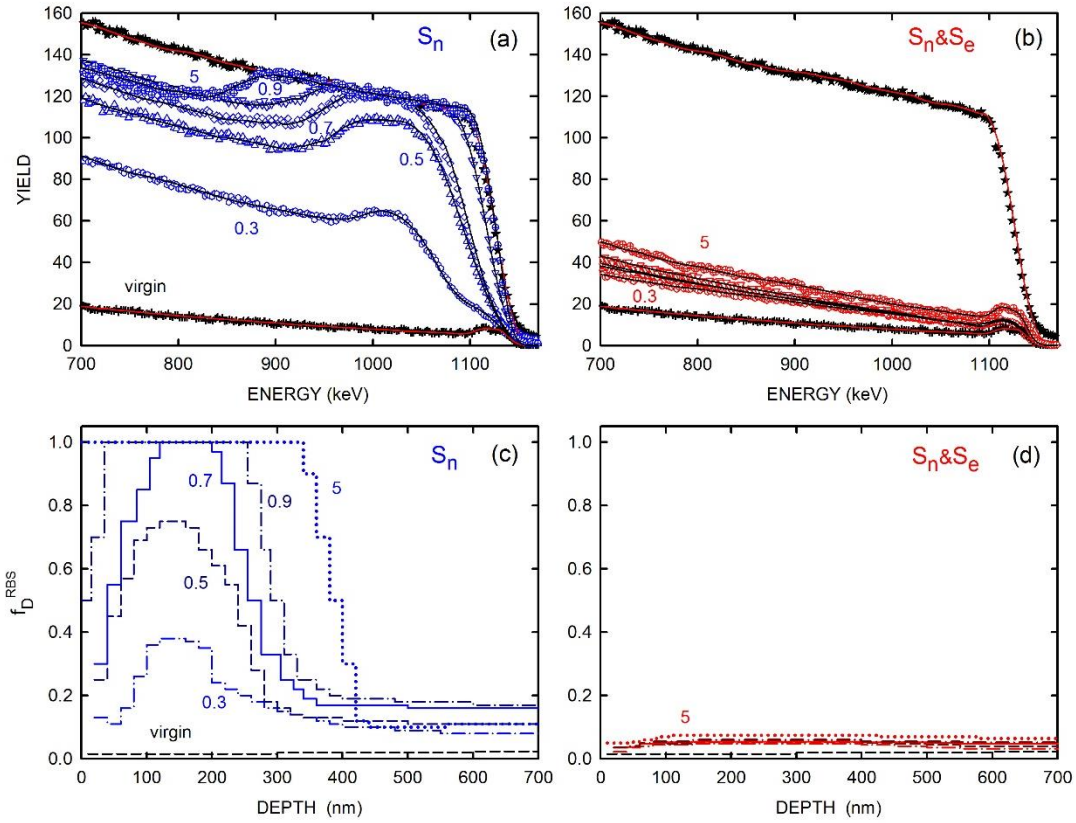

Figure 2

RBS spectra measured in random (black stars) and axial (other symbols) orientations on GaAs crystals irradiated with 900 keV I^{2+} ions (a) or with 900 keV I^{2+} ions & 27 MeV Fe^{9+} ions (b). The numbers are the I^{2+} fluences (in nm^{-2}) used for irradiations. Solid lines are fits to data with the McChasy program [29].

Damage fraction (f_D^{RBS}) *vs* depth obtained from the fits to RBS/C data for GaAs crystals irradiated with 900 keV I^{2+} ions (c) or with 900 keV I^{2+} ions & 27 MeV Fe^{9+} ions (d) at the indicated I^{2+} fluences.

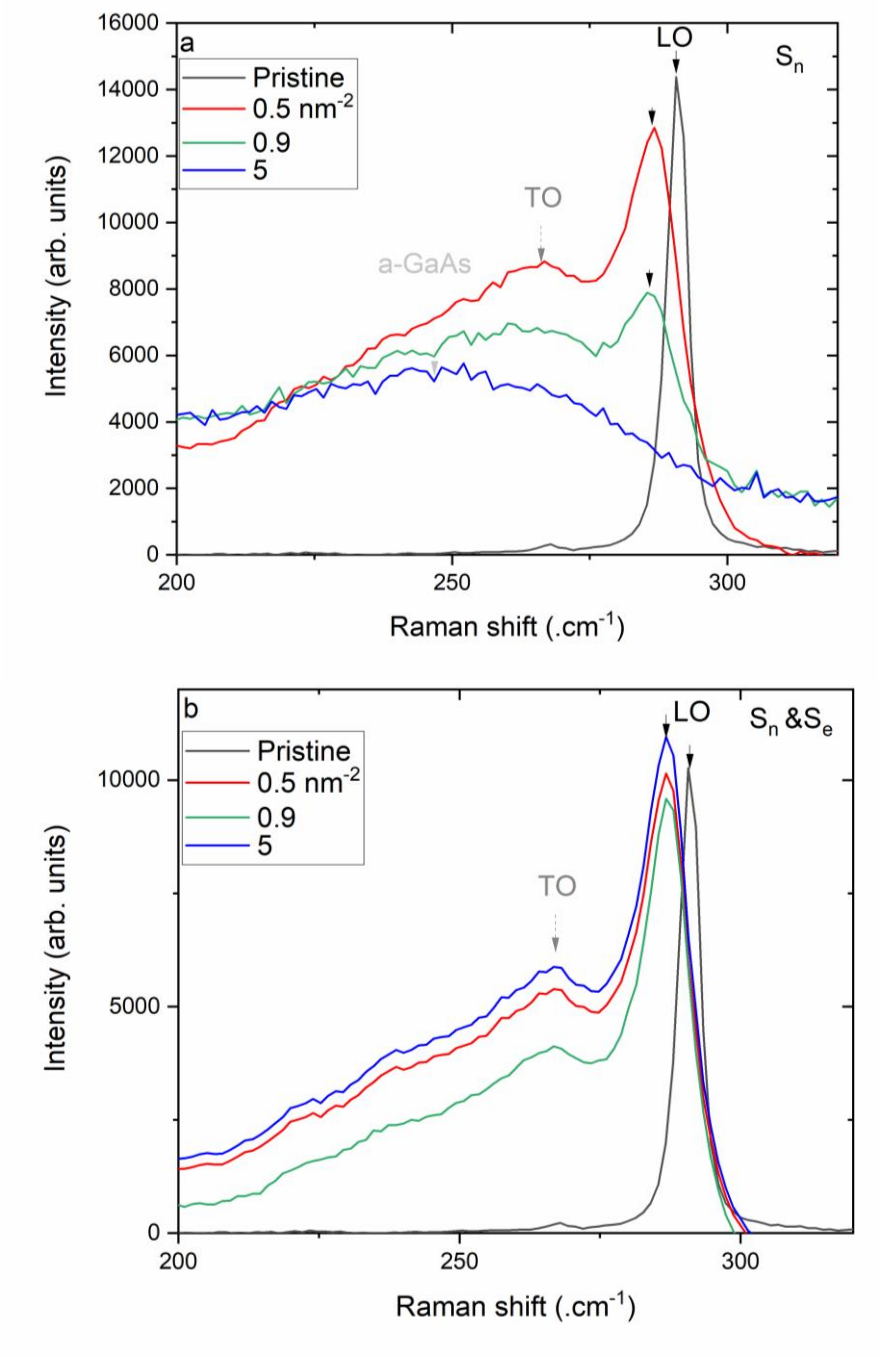

Figure 3

Raman spectra obtained on GaAs crystals irradiated with (a) 900 keV I^{2+} ions (S_n) or (b) 900 keV I^{2+} ions & 27 MeV Fe^{9+} ions (S_n&S_e) at the indicated I^{2+} fluences.

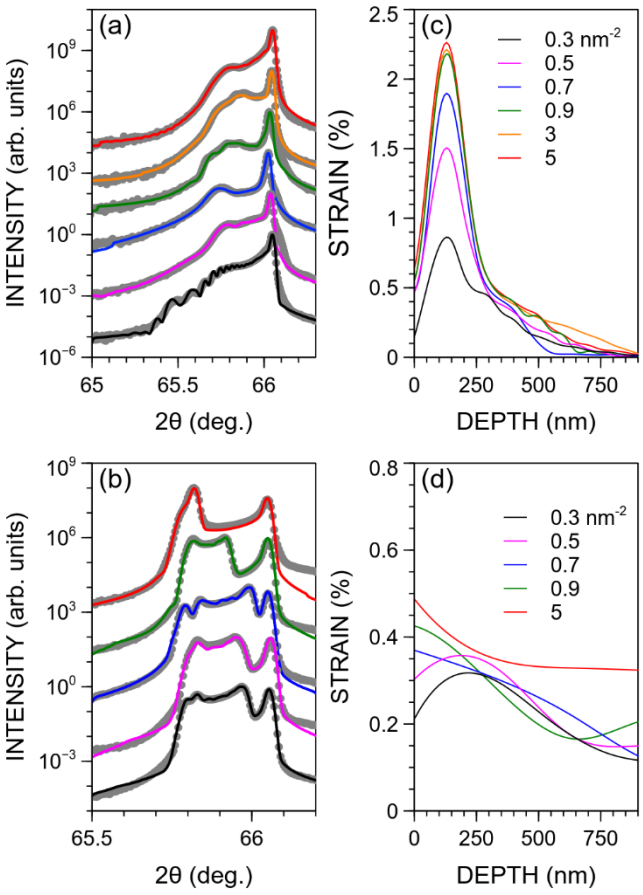

Figure 4

XRD θ-2θ scans obtained around the 400 reflection for irradiated GaAs crystals (gray circles) and associated RaDMaX simulations [30-31] (colored lines), in the case of irradiations with (a) 900 keV I^{2+} ions (S_n) or (b) 900 keV I^{2+} ions & 27 MeV Fe^{9+} ions (S_n&S_e). (c) and (d) display the strain depth profiles derived from the simulations shown in (a) and (b).

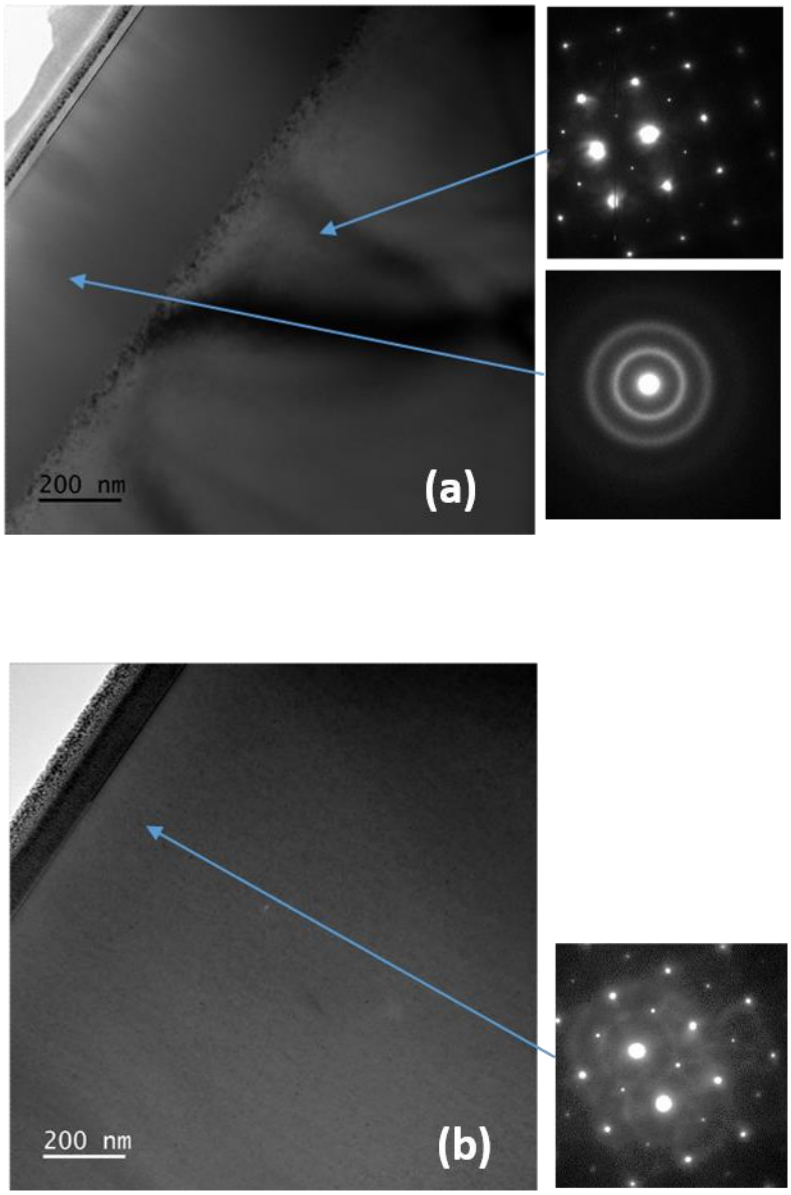

Figure 5

TEM micrographs obtained on GaAs crystals irradiated with (a) 900 keV I^{2+} ions (S_n) at $5x10^{14}$ cm^{-2} and with (b) 900 keV I^{2+} ions & 27 MeV Fe^{9+} ions (S_n&S_e) at $5x10^{14}$ and $9x10^{14}$ cm^{-2}, respectively. The surface is located in the upper left side of the images. Electron diffraction patterns are also presented for selected regions.

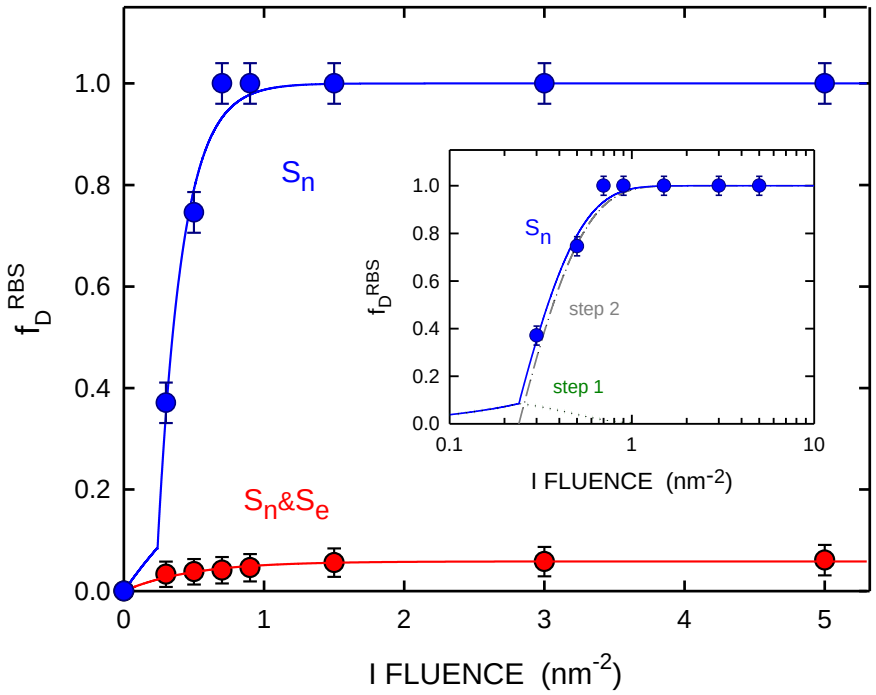

Figure 6

Damage fraction (f_D^{RBS}) *vs* iodine for GaAs single crystals irradiated at RT with 900 keV I^+ ions (S_n-blue circles) or with 900 keV I^+ ions and 27 MeV Fe^{9+} ions. Solid lines are fits to data using the MSDA model (see text).
The inset shows a logarithmic representation of the disorder buildup upon S_n irradiation where the green dotted and grey dashed lines symbolize the steps 1 and 2, respectively, as provided by the MSDA model.

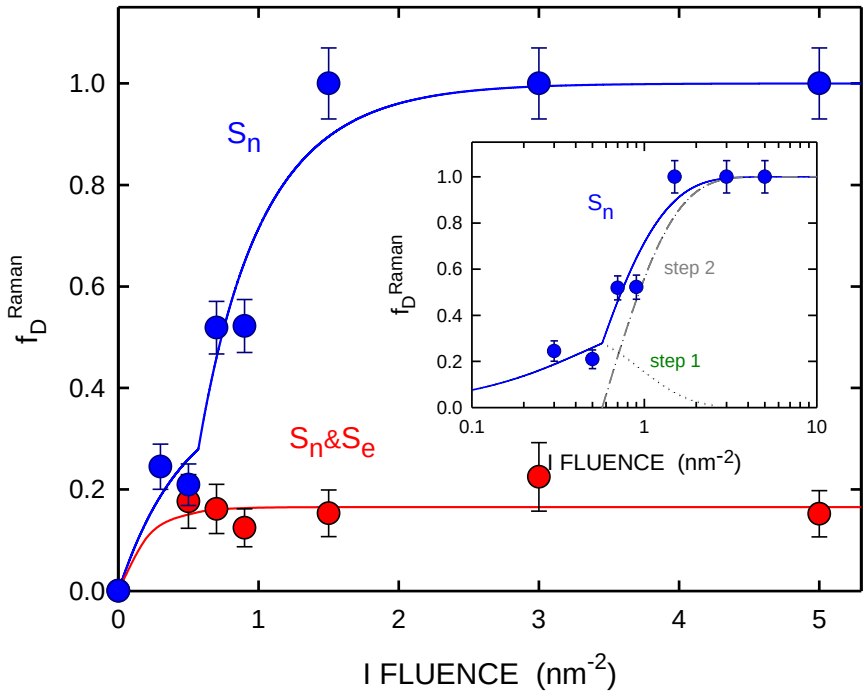

Figure 7

Damage fraction (f_D^{RAMAN}) *vs* iodine fluence for GaAs single crystals irradiated at RT with 900 keV I^+ ions (S_n-blue circles) or with 900 keV I^+ ions and 27 MeV Fe^{9+} ions. Solid lines are fits to data using the MSDA model (see text).
The inset shows a logarithmic representation of the disorder buildup upon S_n irradiation where the green dotted and grey dashed lines symbolize the steps 1 and 2, respectively, provided by the MSDA model.

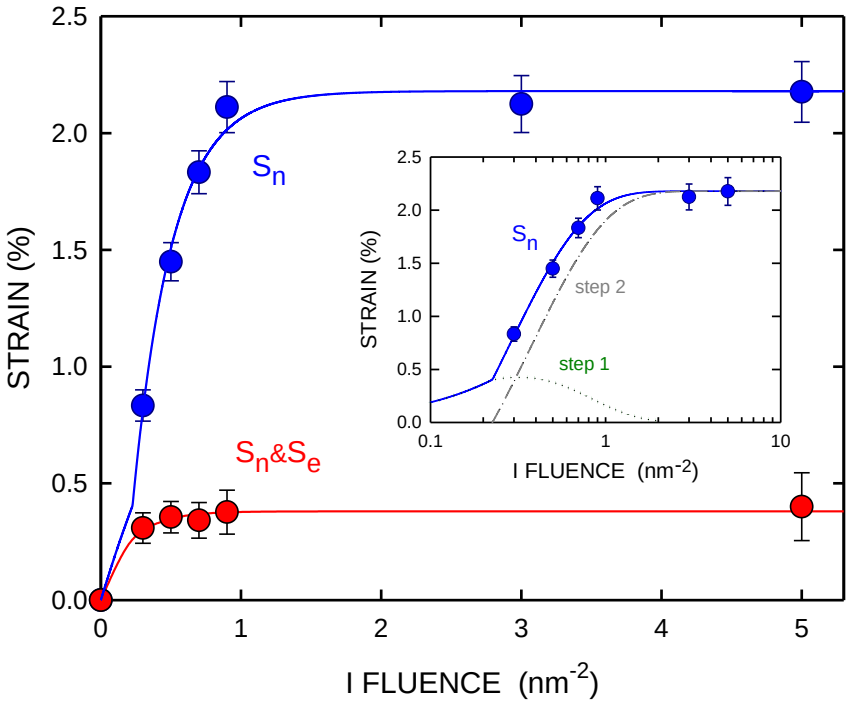

Figure 8

Strain *vs* iodine fluence for GaAs single crystals irradiated at RT with 900 keV I^+ ions (S_n-blue circles) or with 900 keV I^+ ions and 27 MeV Fe^{9+} ions (S_n&S_e-red circles). Solid lines are fits to data using the MSDA model (see text).
The inset shows a logarithmic representation of the disorder buildup upon S_n irradiation where the green dotted and grey dashed lines symbolize the steps 1 and 2, respectively, provided by the MSDA model.

References

[1] P. Rudolph, M. Jurisch, J. Crystal Growth 198-199 (1999) 325.
[2] Brozel M. (2006) Gallium Arsenide. In: Kasap S., Capper P. (eds) Springer Handbook of Electronic and Photonic Materials. Springer Handbooks. Springer, Boston, MA.
[3] J. Chatterjee, International Conference on Trends in Electronics and Informatics, IEEE 978-1-5090-4257-9 (2017).
[4] V.-T. Rangel-Kuoppa, S. Ye, Y.J. Noori, W. Holmkvist, R.J. Young, D. Muenstermann, JINST 16 P09012 (2021).
[5] T. Takamoto, M. Kaneiwa, M. Imaizumi, M. Yamaguchi, Prog. Photovolt: Res. Appl. 13 (2005) 495.
[6] Y. Jestin, Comprehensive Renewable Energy, Volume 1, Chap. 1.26 (2012) 563. Elsevier.
[7] Wesch W, Schnohr C.S (2016) Ion Beam Modification of Solids, chap. 9, ed Springer International Publishing, Switzerland.
[8] Zhang Y, Weber W J (2020) Ion irradiation and modification: The role of coupled electronic and nuclear energy dissipation and subsequent nonequilibrium processes in materials Appl. Phys. Rev. 7:041307.
[9] L. Thomé, G. Velisa, S. Miro, A. Debelle, F. Garrido, G. Sattonnay, S. Mylonas, P. Trocellier, Y. Serruys, J. Appl. Phys. 117 (2015) 105901.
[10] L. Thomé, G. Gutierrez, I. Monnet, F. Garrido, A. Debelle, J. Mater. Sci. 55 (2020) 5938.
[11] M. W. Bench, I. M. Robertson, M. A. Kirk, I. Jencic, J. Appl. Phys. 87 (2000) 49.
[12] R. A. Brown, J. S. Williams, Phys. Rev. B 64 (2001) 155202.
[13] W. Wesch, E. Wendler, C.S. Schnohr, NIM B 277 (2012) 58.
[14] K Nordlund, J Peltola, J Nord, J Keinonen, RS Averback, J. Appl. Phys. 90 (2001) 1710.
[15] J. Nord, K. Nordlund, J. Keinonen, Phys. Rev. B 65 (2002) 165329.
[16] M. Jiang, H. Y. Xiao, S. M. Peng, G. X. Yang, Z. J. Liu, X. T. Zu, Scientific Reports 8 (2018) 2012.
[17] K. Thommen, Radiat. Eff. 2 (1970) 201.
[18] O. Herre, E. Wendler, N. Achtziger, T. Licht, U. Reislijhner, M. Riib, T. Bachmann, W. Wesch, P.I. Gaiduk, F.F. Komarov, NIM B 120 (1996) 230.
[19] A. Kamarou, W. Wesch, E. Wendler, Phys. Rev. B 78 (2008) 054111.
[20] S. A. Goodman, F. D. Auret, G. Myburg, Appl. Phys. A 59 (1994) 305.
[21] I. Jenčič, M. W. Bench, I. M. Robertson, M. A. Kirk, J. Appl. Phys. 78 (1995) 974.
[22] I. Jenčič, Eric P. Hollar, Ian M. Robertson, AIP Conference Proceedings 680 (2003) 701.
[23] D. Kabiraj, S. Ghosh, J. Appl. Phys. 109 (2011) 033701.
[24] L. Thomé, A. Debelle, F. Garrido, P. Trocellier, Y. Serruys, G. Velisa, S. Miro, Appl. Phys. Lett. 102 (2013) 141906.
[25] A. Gentils, C. Cabet, Nucl. Instr. Meth. B 447 (2019) 107.
[26] L. Thomé, G. Gutierrez, I. Monnet, F. Garrido, A. Debelle, J. Mater. Sci. 55 (2020) 5938.
[27] J.F. Ziegler, J.P. Biersack, U. Littmark U (1985) The Stopping and Range of Ions in Solids, Pergamon, New York, available at: www.srim.org.
[28] N. Chen, S. Gray, E. Hernandez-Rivera, D. Huang, P. D. LeVan, F. Gao, J. Mater. Res. 32 (2017) 1555.
[29] L. Nowicki, A. Turos, R. Ratajczak, A. Stonert, F. Garrido, Nucl. Instr. Meth. B 240 (2005) 277.
[30] Souilah M, Boulle A, Debelle A (2016) RaDMaX: a graphical program for the determination of strain and damage profiles in irradiated crystals J. Appl. Cryst. 49:311-316.
[31] A. Boulle, V. Mergnac, J. Appl. Cryst. 53 (2020) 587.
[32] K. K. Tiong, P. M. Amirtharaj, F. H. Pollak, Appl. Phys. Lett. 44 (1984) 1.
[33] U.V. Desnica, D. Desnica, M. Ivanda, T.E. Haynes, NIM B 120 (1996) 236.
[34] A. Debelle, A. Declémy, Nucl. Instr. and Methods B 268, (2010) 1460.
[35] A. Boulle, A. Debelle, J. Appl. Cryst. 43, (2010) 46.
[36] M. Holtz, R. Zallen, O. Brafman, S. Matteson, Phys. Rev. B 37 (1998) 4609.
[37] V. S. Speriosu, B. M. Paine, M. A. Nicolet, Appl. Phys. Lett. 40 (1982) 604.
[38] J. Jagielski, L. Thomé, Applied Physics A 97 (2009) 147.
[39] A. Pillukat, K. Karsten, P. Ehrhart, Phys. Rev. B. 53 (1996) 7823.

[40] K. Nordlund, J. Peltola, J. Nord, J. Keinonen, R. S. Averback, J. Appl. Phys. 90 (2001) 1710.
[41] S. Tian, C. He, H. He, W. Liao, Y. Bai, Y. Li, Comp. Mater. Science 202 (2022) 111016.
[42] M. Mikou, R. Carin, P. Bogdanski, P. Marie, J Phys. III France 7 (1997) 1661.
[43] G. Szenes, Z. E. Horvath, B. Pécz, F. Paszti, L. Toth, Phys. Rev. B 65 (2002) 045206.
[44] A. Colder, B. Canut, M. Levalois, P. Marie, X. Portier, S. M. M. Ramos, J. Appl. Phys. 91 (2002) 5853.
[45] K D Chtcherbatchev, V T Bublik, A S Markevich, V N Mordkovich, E Alves, N P Barradas, A D Sequeira, J. Phys. D: Appl. Phys. 36 (2003) A143–A147.
[46] J. Jencic, E. P. Hollar, I. M. Robertson, Phil. Mag. 83 (2003) 2257.
[47] D. Kabiraj, S. Ghosh, J. Appl. Phys. 109 (2011) 033701.
[48] W. Wesch, A. Kamarou, E. Wendler, K. Gärtner, P.I. Gaiduk, S. Klaumünzer, NIM B 206 (2003) 1018.
[49] L. Thomé, G. Velisa, S. Miro, A. Debelle, F. Garrido, G. Sattonnay, S. Mylonas, P. Trocellier, Y. Serruys, J. Appl. Phys. 117 (2015) 105901.
[50] F. Spaepen, D. Turnbull, Laser-Solid Interactions and Laser Processing, edited by S. D. Ferris, H. J. Leamy, and J. M. Poate, AIP, New York, 1979, p. 73.
[51] M. Toulemonde, W. Assmann, C. Dufour, A. Meftah, F. Studer, C. Trautmann, Mat. Fys. Medd. 52 (2006) 263.
[52] A. Debelle, M. Backman, L. Thomé, W. J. Weber, M. Toulemonde, S. Mylonas, A. Boulle, O. H. Pakarinen, N. Juslin, F. Djurabekova, K. Nordlund, F. Garrido, and D. Chaussende, Phys. Rev. B 86 (2012) 100102 (R).
[53] A. Debelle, L. Thomé, I. Monnet, F. Garrido, O. H. Pakarinen, W. J. Weber, Phys. Rev. Mater. 3 (2019) 063609.
[54] Y. Zhang Y, W. J. Weber, Appl. Phys. Rev. 7 (2020) 041307.
[55] M. W. Bench, I. M. Robertson, M. A. Kirk, I. Jencic, Jour. Appl. Phys. 87 (2000) 49.

Appendix A: SRIM-derived I ion range and corresponding dpa depth profile

Figure 9 presents the I ion range (given in %), and the corresponding dpa depth distribution, for an iodine fluence of 5 nm^2. The dpa peak is found at ~150 nm, while the mean projected range is around 230 nm. The maximum I concentration is less than 0.06 %, and the dpa peaks at almost 13.

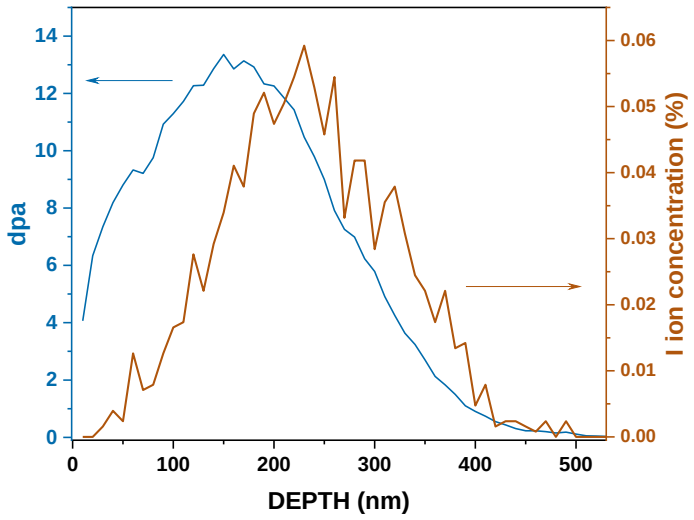

Fig. 9

SRIM-predicted 900 keV I^{2+} ion range, and corresponding dpa depth profile, for an iodine fluence of 5 nm^2. SRIM calculations were performed in the "Full damage cascade" mode.

Appendix B: Comparison between sequential and simultaneous irradiation experiments

Figure 10 represents the damage fraction determined by RBS/C in GaAs irradiated under 4 different conditions: (i) S_n only (blue), (ii) S_e only (green), (iii) S_e subsequent to S_n (S_n+S_e – grey) and (iv) concomitant S_n and S_e (S_n&S_e - red). As explained in the main text, S_n irradiation alone leads to full amorphization of the layer, while during S_n&S_e experiment, the disorder level remains very low. Two other information can be obtained from Fig.10: S_e induces only an extremely weak disorder level, and for a sequential irradiation (S_n+S_e), a shrinkage of the amorphous layer is noticed, but this layer remains essentially amorphous. Hence, the sequential experiment is much less efficient in terms of damage annealing than is the simultaneous one.

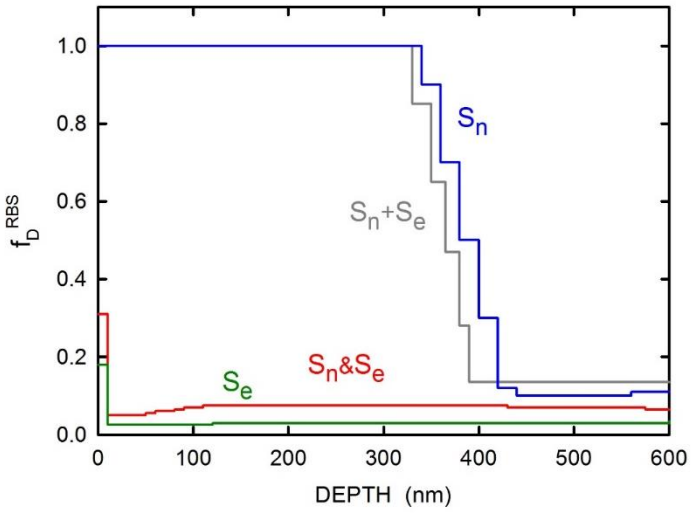

Fig. 10

Damage fraction (f_D^{RBS}) *vs* depth for GaAs crystals irradiated with: a single 900 keV I^{2+} ion beam (S_n - blue line), a single 27 MeV Fe^{9+} ion beam (S_e - green line), dual 900 keV I^{2+} & 27 MeV Fe^{9+} ion beams (S_n&S_e - red line), sequential single 900 keV I^{2+} and 27 MeV Fe^{9+} ion beams (S_n+S_e - grey line).